Experimental Mechanics (2010) 50:1199–1212
DOI 10.1007/s11340-009-9323-9

Mode I Fracture at Spot Welds in Dual-Phase Steel: An Application of Reverse Digital Image Correlation

H. Tao · P.D. Zavattieri · L.G. Hector Jr. · W. Tong

Received: 4 April 2009 / Accepted: 21 December 2009 / Published online: 26 January 2010

Abstract Strain fields in 600 grade dual-phase steel V-notch tensile specimens, both with and without a spot weld, were measured after mode I fracture initiation. Starting with the final image of a fully developed crack, a novel reverse digital image correlation (DIC) analysis was used to determine the path that the crack followed at the onset of fracture as well as the crack tip deformation field. This gave the pixel coordinates of grid points on both sides (i.e. fracture surfaces) of the crack path in the undeformed image. Strain fields that develop in the base material regions surrounding the two fracture surfaces were subsequently measured with forward DIC analysis. Steady state values of the crack tip opening displacement (CTOD) and crack tip opening angle (CTOA), which are important fracture parameters, were measured for the base DP600 metal. Notch tip opening displacement (NTOD) and notch tip opening angle were also measured. It was found that steady state values of the CTOD and CTOA are reached within 2 mm or so of crack growth following completion of the flat-to-slant transition of the fracture surface and stabilization of the crack tunneling effect.

Keywords Reverse digital image correlation · Mode I fracture · Spot welds · DP steel

H. Tao
Mechanical Engineering Department, Yale University,
New Haven, CT 06520, USA

P.D. Zavattieri (✉)
School of Civil Engineering, Purdue University,
West Lafayette, IN 47907-2051, USA
e-mail: zavattie@purdue.edu

L.G. Hector Jr.
General Motors Research and Development,
30500 Mound Road,
Warren, MI 48090-9055, USA

W. Tong
Department of Mechanical Engineering,
Southern Methodist University,
Dallas, TX 75275, USA

H. Tao
Hong Kong Productivity Council, HKPC Building,
78 Tat Chee Avenue,
Kowloon, Hong Kong

Introduction

Substantial effort has been directed toward the development of dual-phase (DP) steels for applications in transportation industries [1–3]. The unique mechanical behavior of DP steels includes continuous yielding, a low yield/tensile ratio, a high rate of work hardening, and high uniform and total elongation [4]. The term "dual-phase steel" refers to the predominance of two phases in the ferrous microstructure, viz., the relatively soft body-centered-cubic ferrite, and the relatively hard body-centered-tetragonal martensite [5–7].

Spot welding is a critical part of vehicle assembly. Finite element (FE) simulations of spot welds in vehicle structures are often based upon component models where the weld is represented by beam or plate elements. These models do not account for weld fracture behavior under the mixed mode conditions to which welds can be subject during impact situations [8].

Variations of material and mechanical properties across a DP spot weld render the optimization of welding process parameters and development of accurate fracture constitutive models extremely challenging [9]. These variations were previously explored for the base metal, heat-affected zone (HAZ) and fusion zone materials in DP 600 spot

welds [10]. Using low strain rate tensile tests with a state-of-the-art digital image correlation technique, material models were generated for all three welds zones. The strength of the fusion zone was shown to exceed that of the base material due the higher martensite fraction in the fusion zone. The material models from [10] were used to accurately predict plastic deformation of single DP600 spot welds in simple tension using finite element analysis [11].

Failure of resistance spot welds is dependent upon complex interactions between a variety factors. Among the more significant are deformation rates and loading path, welding parameters and weld geometry, porosity, sheet thickness, and base, HAZ and fusion zone material properties [9, 12, 13]. Fracture behavior is typically modeled with three-dimensional structural simulations or inferred from simple laboratory tests [14–16] and only relatively simple failure criteria for resistance spot-welds have been used in structural analyses [17]. Validation of existing spot-weld failure criteria has been explored with analytical approaches wherein the stress distribution around a weld is related to the far field failure load [14, 15, 18–23] and with finite element failure simulations [24, 25]. There are numerous reports in the literature aimed at predicting failure of spot welds under various loading conditions such as tension [23], shear [23], combined tensile/shear [16, 23, 26], impact [27], and fatigue [28, 29]. Test specimens with different geometries (e.g. cross-tension, coach-peel, tension-shear, pure-shear as well as button pull-out) have been used to analyze the failure behavior of spot welds under loading paths that are more complex than simple tension. In a recent study [30], a semi-empirical fracture criterion for large (216 mm×38 mm) DP steel simple shear coupons with a single spot was reported. This criterion relates a critical shear force at which fracture initiates to the initial thickness of the spot welded sheets and the ratio of the maximum hardness to the minimum hardness of the HAZ (determined from indentation tests). If the calculated tensile shear force is greater than the critical value, the weld is predicted to fail by button pull-out fracture. Alternatively, if the calculated simple shear force is less than the critical value, then the weld is predicted to fracture via the less desirable interfacial fracture mode. Additional failure models may be found in [16, 26, 27]. Although such studies provide a useful starting point for failure criteria development, fracture material models for DP spot welds must be based upon a more generic approach that consists of accurate strain field measurement. Such measurements can then be used to validate finite element predictions of spot weld deformation and fracture.

This paper presents an experimental methodology that provides strain fields in the vicinity of a propagating crack in DP600 V-notch tensile specimens both with and without a single spot weld. The choice of specimen geometry limited the present study to mode I initiation which is not fully representative of the mixed mode fracture conditions to which spot welds can be subject during vehicle impact [31]. However, the simple V-notch geometry facilitated accurate strain field measurement with a state-of-the-art digital image correlation (DIC) technique which can be subsequently applied to more complex fracture modes and experimental tests [32–36].

CTOD/CTOA for Ductile Fracture

The crack tip opening displacement (CTOD) was first proposed by Wells [37] who observed that sharp crack tips become blunted due to plastic deformation prior to crack propagation. He found that the CTOD achieved a constant value for stable crack growth in metals and that it is essentially a measure of the fracture toughness. The concept of the crack tip opening angle (CTOA) was proposed some time later [38, 39]. It is important to note that application of the CTOD/CTOA criteria assumes a pre-existing sharp crack (of a given length) in the material. Various experimental techniques have been used to measure the CTOA and CTOD in metals [40–44]. More recently, new techniques to measure mixed mode I/III CTOD in ductile aluminum and steel HSLA340 under in-plane and out-of-plane loading conditions using 3D DIC technique have been developed [45–47]. A subset splitting technique using DIC was proposed to measure displacement jumps across the discontinuities to detect crack growth under Mode I and II loading conditions [48].

In FE simulations, crack growth has been modeled with steady state values of the CTOD or CTOA [49]. An initially bonded node pair at the crack tip is separated with the crack then extended by one element to simulate crack growth. Load-crack extension curves are predicted based on the CTOD/CTOA failure criteria. Values of the CTOD in conjunction with a 3D fracture simulation code to analyze crack tunneling in ductile sheet metal have also been used [50]. As a result, it was found that the critical CTOD value has a clear dependence on the crack-front stress triaxiality. Other issues/limitations of the CTOD or CTOA as single fracture criteria that need to be taken into account are the ability to capture crack initiation, crack branching, crack coalescence, and the ductile-to-brittle transition. From the computational implementation point of view (e.g., in a FE code), the need to keep track of each single crack is an important issue. For this, the use of a mesh independent method (e.g. interface element methodologies, mesh-free, X-FEM and adaptive re-meshing) would be desirable.

Additional quantities that can be measured during fracture are the notch tip opening angle (NTOA) and the notch tip opening displacement (NTOD). Both are measured relative to the initial notch-tip position. They can be determined continuously throughout a test without any specific information about the moving crack tip position

[51]. These quantities are generally easier to measure than the CTOA and CTOD. Measurements of CTOD and CTOA of a steady state growing crack first require the current location of the crack tip and then the position at a given distance (typically 1 mm) behind each of the two fracture surfaces. If the NTOA and the NTOD could in principle be quantitatively linked to the CTOA and the CTOD, then there would be less need to measure the latter.

Experimental Details

Dual-Phase Steel (DP600)

Cold-rolled, galvanized, DP600 steel sheets with a 2.0-mm gage were used in this study. The steel supplier was National Steel. Manganese, chromium and carbon were the main alloying elements and their concentrations were comparable to those in other commercial dual-phase steels. The nominal yield and ultimate tensile strengths were 340 MPa and 590 MPa, respectively. The resistance spot welds were fabricated using direct-current and single pulse schedules on two identical overlapping dual-phase steel sheets. Welding current and welding hold time were set to approximately 10 kA and 20 cycles (i.e. 1/3 s), respectively. This combination of welding process parameters was found to consistently generate weld diameters of approximately 6 mm. Note that the HAZ was of the order of 0.5–0.7 mm in width. On average, the hardness of the weld fusion zone, which consisted of 80%-martensite/20%-ferrite was 3.93 GPa. This is about 75% greater than that of the base material (2.37 GPa). The hardness values were obtained using the Oliver-Pharr method from nanoindentation tests [63]. See Ref. [10, 64] for additional details behind the hardness measurement. Further details on the microstructure of the base and fusion zone materials as well as measured properties of these materials may be found in [10, 64].

Fracture Specimen Preparation and Dimensions

All dual phase steel specimens tested in the present work were prepared with precision electrical discharge machining. The 1.7 mm-thick single sheet V-notch specimen with no weld is shown in Fig. 1(a). The notch is 5 mm deep, as indicated in the figure, with a 60° angle. The overall specimen length and width are 56 and 25 mm, respectively. Two-5 mm diameter holes were machined in each specimen to accommodate the loading pins. The centers of the two holes, which were separated by 30 mm, were aligned with the notch tip as detailed in Fig. 1(a). Additional specimen geometries had a single spot weld 1.5 mm beneath the notch tip, as shown in Fig. 1(b), and touching, or slightly penetrating the outer perimeter of a single spot weld, as shown in Fig. 1(c). Each spot weld, which is denoted by the solid circle in Figs. 1(b), (c), had a nominal diameter 6 mm. All surfaces of each fracture specimen were found to be free of obvious machining defects. Figure 2 shows an off-center view of the specimen geometry in Fig. 1(b) where the weld and notch tip are separated by 1.5 mm.

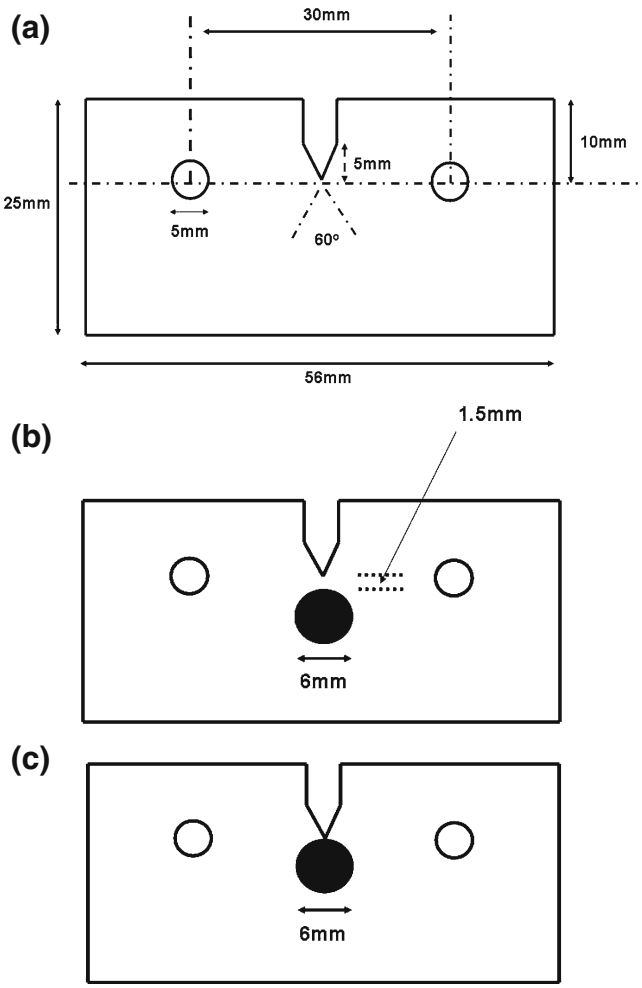

Fig. 1 Schematics of DP600 fracture specimens. (**a**) base material with no spot weld, loading occurs along the dot-dashed line through the loading pin holes; (b) and (c) 1–2 mm-thick DP600 coupon with 5 mm notch and loading pin holes. (**b**) spot welded specimen with spot weld (*solid circle*) positioned 1.5 mm below the notch tip; (**c**) spot welded specimen with notch tip touching the outer perimeter of the spot weld (*solid circle*). Each spot weld had a 6 mm nominal diameter, as indicated

Fracture Testing

The experimental configuration for the fracture tests, which is shown schematically in Fig. 3(a), consisted of three main components:

(1) An MTS 810 (hydraulic) tensile-testing machine for load application under a constant cross-head speed;
(2) Imaging equipment for digital image acquisition and additional processing;
(3) A data acquisition computer.

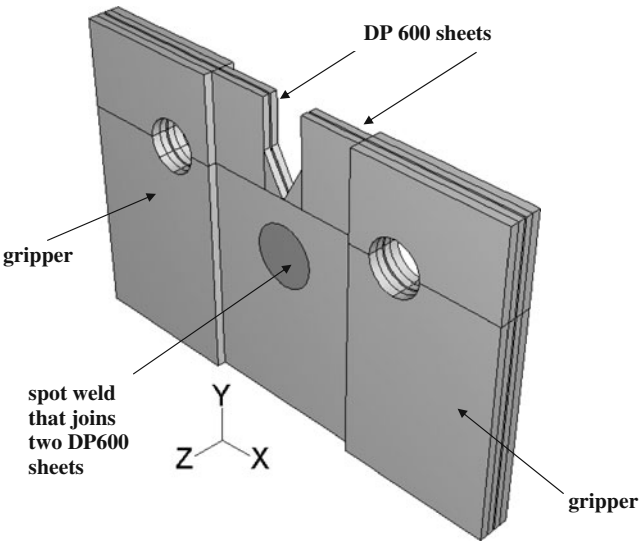

Fig. 2 Off-center view of a single weld V-notch specimen in Fig. 1 (b). Spot weld is positioned 1.5 mm beneath the notch tip

The testing instrumentation electronics allowed for load data acquisition at 8 Hz. The MTS machine had a load cell with a capacity of 20,000 N and a displacement transducer with a measurement range of 100 mm. The cross-head speed used in these experiments was 0.01 mm/s, and the load data sampling rate was 8 Hz. Figures 3(b), (c) show the experimental configuration and a close-up view of the grippers in the MTS machine, respectively. Note the DP600 V-notch specimen at the center of the grippers in Fig. 3(c). One surface of each specimen was decorated with a pattern of black and white paint speckles. The decorated surface of each fracture specimen was imaged continuously at 8 s intervals during the tests with a Canon Rebel digital camera. A set of 3072×2048 pixel digital images of the whole area in the vicinity of the crack tip was recorded with a spatial resolution of 21.5 μm/pixel. The size of a typical contrast feature or speckle was about 10 pixels. The time history was logged by tracking the stepping number of the stepping motor and then associating recorded axial load and displacement of the tensile testing apparatus with a given stepping number. The image and load data were then synchronized for post-processing with DIC. The fracture surfaces were examined with SEM to provide microstructural details about the fracture process.

Deformation Measurment and Reverse DIC

Background

The DIC-based deformation measurement technique [36] was used to measure crack tip deformation fields, deformation in the regions bounded by the fracture surfaces, and the CTOD/CTOA, and NTOD/NTOA variations with crack length. A variation of the DIC technique, referred to as "reverse DIC," was applied to measure steady state values of the CTOD/CTOA and NTOA/NTOA, and crack-tip deformation fields [35, 44, 52]. Although the CTOD/CTOA have been investigated in welds of other materials [53–56], no existing studies of spot weld fracture in DP steels with the CTOD/CTOA could be identified during the course of the present investigation (a similar observation holds for other advanced high strength steels). A general description of the DIC measurement methodology has been detailed elsewhere [10, 11, 36]. The measurement procedures are briefly described here.

Crack Tip Deformation Field

A close-up image (#1704) of a typical undeformed V-notch specimen (consisting entirely of base DP600 material) mounted in the testing stage is shown in Fig. 4(a). The loading direction is along the vertical direction in the image. When characterizing the deformation field during fracture, an area that surrounds the crack tip must be selected over which strain field measurements are to be made. This area is delimited by the solid white boundary lines that follow the notch geometry. The horizontal dashed white line and yellow dotted lines represent the as-of-yet unknown crack surfaces. The information that must be obtained to determine these surfaces during fracture are the pixels corresponding to the horizontal dashed white line and yellow dotted lines (i.e. the crack surfaces) in the undeformed image of Fig. 4(a). The same bounding area in Fig. 4(a) is shown in Fig. 4(b) (image #1760) which is the specimen in Fig. 4(a) at a later stage of mode I fracture. As the crack grows from the notch in mode I fracture, free boundaries of the specimen, which are delimited by the same dashed white and dotted yellow lines, were formed. One cannot carry out the conventional DIC using Fig. 4(a) (as the reference image) and Fig. 4(b) (as the current image) since a continuous displacement field with a pixel subset is assumed and this does not address a pixel subset across the crack boundaries (where there is no material). In other words, comparison of the image in Fig. 4(a) (as the reference image) with that in Fig. 4(b) will not yield any useful displacement or strain information in material that surrounds the crack boundaries due to the open (black) region between the crack surfaces in the latter. Hence, a region of interest (i.e. the image region that contains the discrete grid points computed in the post-processing step at which displacements and strains are to be measured) cannot be defined without prior knowledge of the crack geometry, and in particular, the location of its tip and free boundaries.

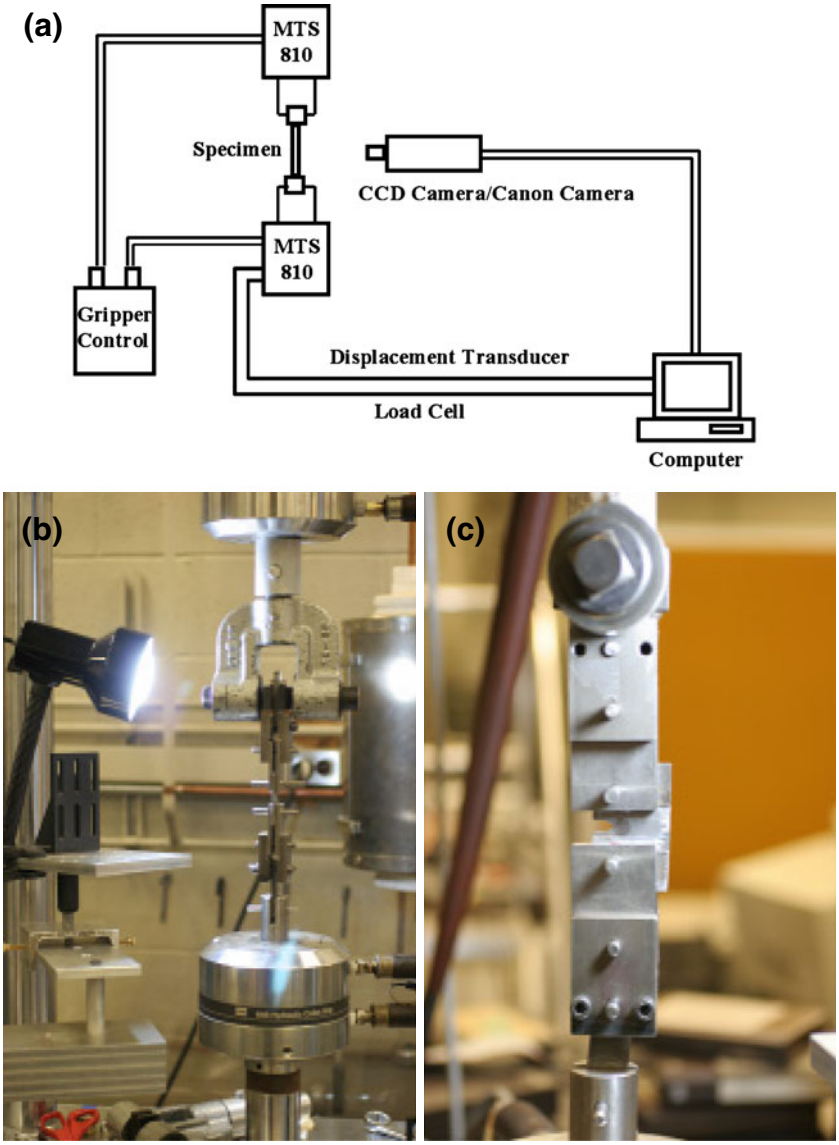

Fig. 3 (**a**) Schematic of experimental setup for fracture testing; (**b**) MTS machine; (**c**) grippers used to deform each fracture specimen. Loading occurs along the vertical direction in the image

Reverse DIC

The difficulties described in "Crack Tip Deformation Field" can be readily overcome by using the so-called reverse DIC analysis approach. The reverse DIC method that we apply to crack-tip deformation field measurement for a growing crack has been used in other applications reported in the literature [35, 48, 62]. In this paper, we use reverse DIC to automatically find the pixel coordinates of the upper and lower free surfaces of the growing crack on the undeformed image and then use them in two separate forward DIC analyses of the entire image set for obtaining ductile fracture parameters CTOA and CTOD. This approach is unique in that the actual path of a growing ductile crack is explicitly identified for uncracked images. Using image #1760 in Fig. 4(b) as the reference image (for example), with well-defined free boundaries of the grown crack, and the undeformed configuration in Fig. 4(a) as the current image (#1704), the continuity assumption on the subset deformation will always be valid. Therefore, in the reverse DIC method, the pixels corresponding to the crack surfaces in Fig. 4(b) are located in the initial undeformed image of Fig. 4(a). These pixels correspond to the "interface" denoted by the dashed white and dotted yellow lines in Fig. 4(a). Once these are known in Fig. 4(a), then a suitable region of interest (over which strain fields can be computed) is defined and forward DIC is then used (starting with Fig. 4(a) as the reference image) to compute deformation fields in material bounded by the crack surfaces.

Figure 4(c) shows a schematic of the region over which reverse DIC analysis was conducted; this is bounded by the crack boundaries in Fig. 4(b). This region was chosen at some distance from the left edge of the specimen, as shown in Fig. 4(b), so as to avoid any bending effects. It is large

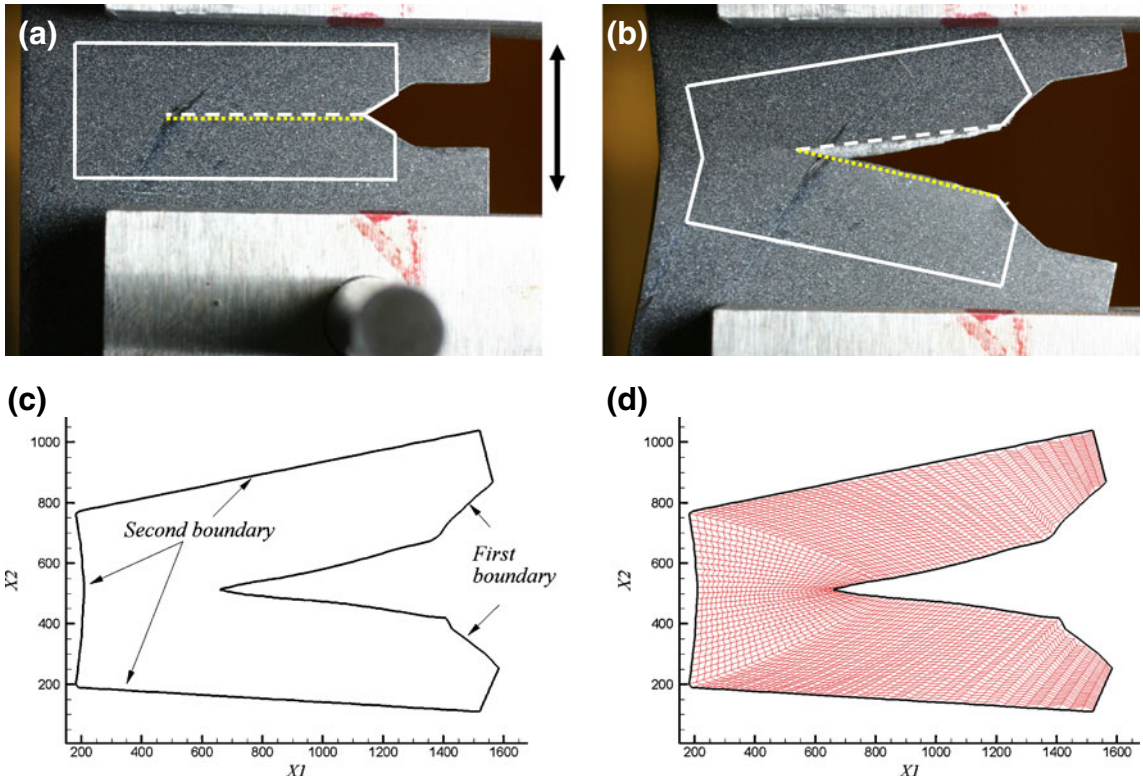

Fig. 4 Illustration of the DIC processing region for a crack tip deformation field (base metal fracture coupon GMT170). (**a**) The corresponding undeformed image #1704 prior to crack initiation along with the crack path (solid white dashed and yellow dotted lines) computed from reverse DIC. The loading direction along X2 is denoted by the double arrow. (**b**) The deformed image (#1760) of the fracture coupon with a grown crack. The region of interest is outlined by thick white lines enclosing the crack tip. The upper and lower crack surfaces are denoted solid white dashed and yellow dotted lines, respectively. The image size is 3072-by-2048 pixels and the image spatial resolution is 21.5 μm/pixel. (**c**) The outline of the region of interest and the two sets of boundaries used for generating a non-uniform grid point set. X1 and X2 are the horizontal and vertical pixel coordinates of the digital image. (**d**) The entire grid point set used in the reverse DIC calculations between the deformed image #1760 and the undeformed image #1704. Each grid point is located at the intersection of crossing mesh lines (*including the region boundary lines*). Results of the reverse DIC analysis of images #1760 and #1704 are given in Fig. 7

enough to include significant variations in plastic deformation around the crack tip. The first set of boundary lines (denoted by "First boundary" and including the notch and crack surfaces) as shown in Fig. 4(c) was formed by a set of adaptively spaced grid points. These are shown explicitly in Fig. 4(d). The second set of boundary lines (denoted by "Second boundary") as shown in Fig. 4(c), was also defined by adaptively spaced grid points of the same total number.

The entire grid point set used in the reverse DIC analysis is shown in Fig. 4(d). The interior grid points were specified along straight lines drawn to connect the corresponding grid points on the two sets of boundary lines [i.e. the "First" and "Second" boundaries as shown in Fig. 4(c)]. Each point at the intersection of two lines in Fig. 4(d) defined an interior grid point used in the DIC analysis to obtain local displacement and strain values. Hence, the reference image was the "cracked" V-notch specimen with the geometry shown in Fig. 4(d) near the end of the fracture test. Displacement and strain fields were computed via comparison of positions of the grid in Fig. 4(d) of the reference image #1760 with those computed in Fig. 4(a). In this way, the cumulative deformation history was effectively obtained in the reverse order from the end to the start of the test (i.e. as the crack closes to the initial undeformed state in Fig. 4(a)). Representative results of the reverse correlation analysis associated with the reference image #1760 in Fig. 4(b) and the current image #1704 in Fig. 4(a) are shown in Fig. 7(f) (after a correction procedure detailed in Tong, 2004b).

CTOD, CTOA, NTOD, NTOA

Definitions of the crack tip opening displacement (CTOD), crack tip opening angle (CTOA), notch tip opening displacement (NTOD), and notch tip opening angle (NTOA) are listed in Table 1. The reference points associated with these definitions are depicted in the schematics of Figs. 5(a), (b), respectively. In Fig. 5(a), points "A" through "H" pertain to the undeformed configuration (i.e. the notch prior to crack initiation). Points "a" through "h" in Fig. 5(b) correspond to the deformed configuration. Here, point "A" in the undeformed config-

Table 1 Definitions of CTOD/CTOA and NTOD/NTOA (see Fig. 5(b))

$CTOD = U_d - U_c$ (2a) $NTOD = U_b - U_a$ (2b)	U is the absolute displacement calculated by DIC in the loading direction for a grid point.
$CTOA = 2\tan^{-1}\left(\frac{CTOD-U_{ef}}{2L}\right)$ (3a) $NTOA = 2\tan^{-1}\left(\frac{NTOD-U_{gh}}{2l}\right)$ (3b)	U_{ef} is the relative separation of two points at the identified crack tip; U_{gh} is the relative separation of points g and h behind the original notch tip [Fig. 5(b)]. Note that L and l are the lengths measured from the crack tip and notch tip, respectively (both are 1 mm in Fig. 5(b)).

uration corresponds to point "a" in the deformed configuration, and so on. Figure 5(a) shows the undeformed configuration where line $\overline{ECGA}$ is the upper crack surface (denoted by the dashed white line in Fig. 4(a)) and $\overline{FDHB}$ is the lower crack surface (denoted by the dotted yellow line in Fig. 4(a)). Figure 5(b) shows the deformed configuration with crack tip blunting (denoted by the curved section between points "e" and "f") associated with DP600. Note

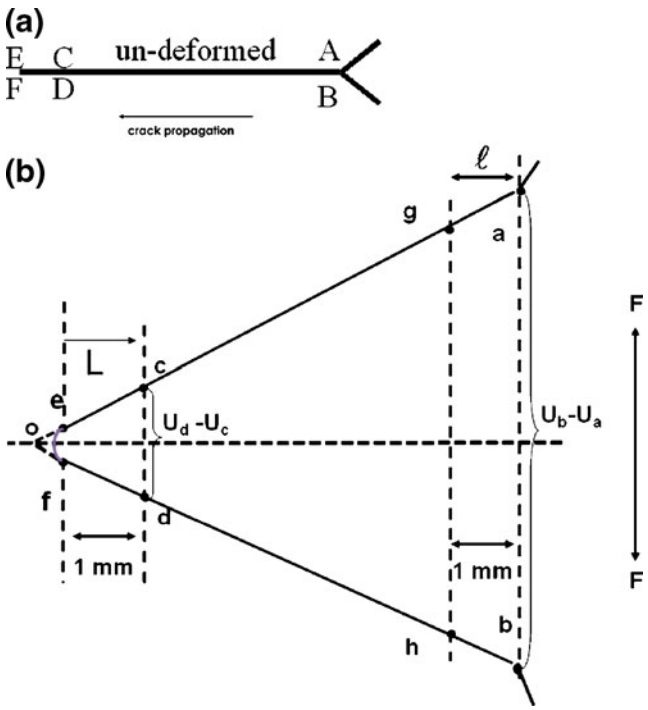

Fig. 5 Schematics associated with the definitions of CTOD/CTOA and NTOD/NTOA for the V-notched mode I fracture specimen: (**a**) undeformed configuration showing initial positions of the crack boundary lines A-G-C-E and B-H-D-F; (**b**) deformed configurations with crack tip blunting (*small curved region between "e" and "f"*), the crack edge is defined by lines a-g-c-e and b-h-d-f. The loading direction is indicated by the double arrow

that the sharp or "ideal" crack tip is positioned at "o", rather than the blunted region between points "e" and "f". Lines $\overline{ecga}$ and $\overline{fdhb}$ define the actual open crack surfaces (or, alternatively, the crack-edge lines or crack-boundary lines), with $\overline{ecga}$ corresponding to the dashed white line in Fig. 4(b), and $\overline{fdhb}$ corresponding to the dotted yellow line in Fig. 4(b). The CTOD is defined as the relative normal separation of the two points "c" and "d" in Fig. 5(b) measured 1-mm behind (i.e., L=1 mm) the nominal crack-tip at points "e" and "f" in Fig. 5(b) (this was identified via visual inspection of the digital images). The NTOD is defined as the relative normal separation of points "a" and "b" in Fig. 5(b) (the original notch tip).

Application of DIC to the measurement of the CTOD and CTOA is not new (see, for example [41]). However, the CTOA defined here is different from that used in previous references [40, 41, 57]. The definition of the CTOA in equation (3a) is based upon the observation (e.g., when one examines the images in Fig. 7(e) and g at high magnifications) that the crack tip may not be perfectly sharp, but in fact may blunt prior to growth. Therefore, when calculating the CTOA based on the displacements obtained from DIC analysis, the relative separation at the nominal crack tip "e" and "f" must be eliminated. In other words, the CTOA may not be calculated from the triangle formed by the ideal crack tip and two points at the measurement location (1-mm behind the ideal crack tip) as the location of ideal crack tip may not be accurately determined. The CTOA would be overestimated if it were directly calculated from the CTOD without subtracting the relative separation of the two points at the nominal crack-tip U_{ef}, i.e., using the conventional approach [41, 57]

$$CTOA = 2tan^{-1}\left(\frac{CTOD}{2L}\right), \tag{4}$$

where L is a fixed distance (e.g., L=1 mm) behind the visible crack tip. A similar definition of NTOA is used via equation (3b) in Table 1, where "g" and "h" are at a location 1-mm ahead (i.e., l=1 mm) of the original notch tip [i.e. points "a" and "b" in Fig. 5(b)].

Figure 6(a) shows the two regions of interest in the undeformed configuration. These were computed in the reverse DIC process. The white and yellow lines in Fig. 4(a) have been replaced by red lines (denoting the upper portion) and black lines (denoting the lower portion). To compute the strain fields that developed in these regions as fracture progressed, forward DIC analyses were conducted on both regions with the customized grids shown in Fig. 6(b) using the entire image sequence of the crack growth process. The positions of both the upper and lower crack edges obtained from the two separate DIC analyses were then used to determine the CTOA, CTOD, NTOA, and NTOD according to Table 1 and Fig. 5(b).

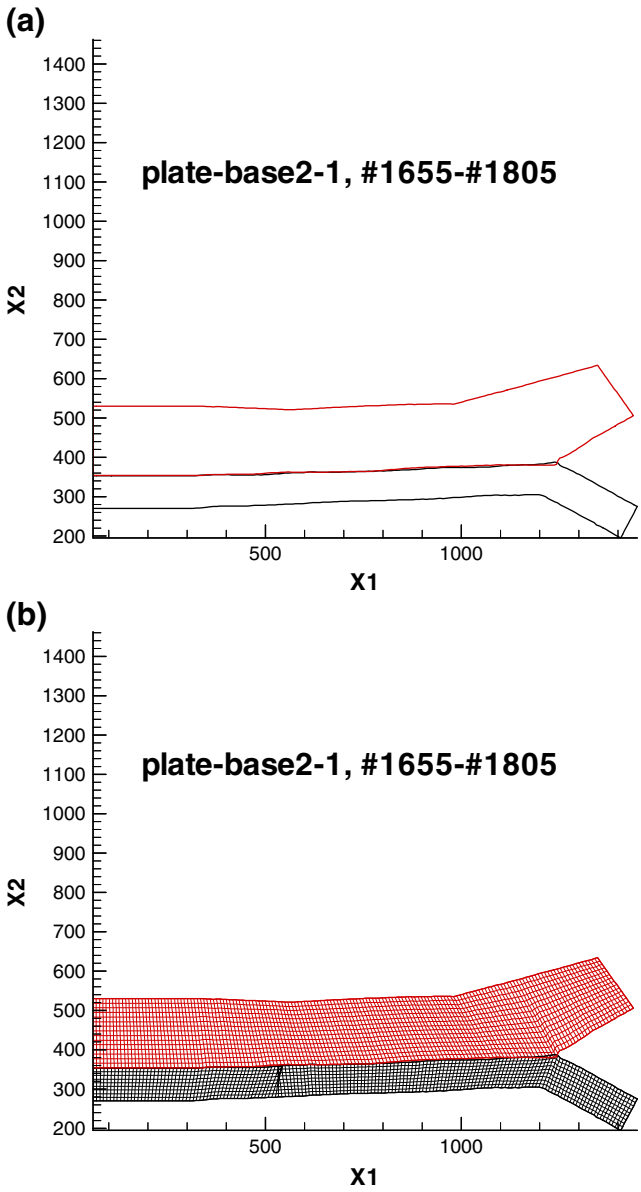

Fig. 6 Illustration of the DIC processing region for computing CTOD/CTOA and NTOD/NTOA (V-notched base metal compact tension coupon No.2-1): (**a**) the two regions of interest defined over the undeformed image #1655 at the start of the fracture test; (**b**) the grid point set defined by the intersection points of crossing mesh lines. X1 and X2 are the horizontal and vertical pixel coordinates of the digital images. Results of two forward DIC analyses of the image pair #1655 and #1805 are given in Fig. 8

Experimental Results

DP600 Base Metal

Four fracture tests were carried out on V-notched compact tension specimens consisting of DP600 base metal. Each was given a unique "BM" label (for "Base Material") in the first column of Table 2. Results from DIC analysis in the SDMAP (Surface Deformation Mapping) program are listed in Table 2. The true plastic strains at notch tip blunting at the outset of the tests are reasonably consistent, with the smallest strain being 28.66% and the largest strain being 37.14%. The threshold CTOA/CTOD values for steady crack growth from the four tests are closely grouped, with average values of 9.57° and 0.49 mm, respectively. A representative DP600 base metal load-displacement curve (where the displacement is the cross-head displacement of the MTS machine) from BM2 is shown in Fig. 7(a). At the maximum load level of 9800 N, the sharp V-notch blunted. This is shown in the digital image in Fig. 7(c). Contours of the computed strain field transverse to the loading direction, Er1, are displayed in the cumulative strain contour map of Fig. 7(d). The accumulated plastic strain immediately ahead of the notch tip is ~30%. A similar strain level was consistently found in the three other V-notch fracture tests summarized in Table 2. Upon further loading, the crack nucleated in the notch and started to grow as shown in Figs. 7(e), (g). Contours of cumulative true strain along the loading direction, Er2, are shown in Figs. 7(f), (h). It is worth noting that the plastic strain at the crack tip slightly decreased with crack propagation (this is not shown in the contour maps). The maximum plastic deformation occurred at the crack tip or blunted notch. At a certain crack length, the Er2 plastic strain contour values along the crack path slightly decreased from the original notch tip [Fig. 7(f)] but increased again at later stages of deformation [Fig. 7(h)]. The tests were terminated after a period of stable crack growth so as to avoid substantial bending at the left end of a test specimen. Note that some compressive strains (blue contours) are seen in Fig. 7(h). These denote the development of small bending strains. The strain fields computed with the cumulative correlation DIC analysis can be used as a basis for validating DP600 fracture models for the base DP600 material.

Table 2 Threshold CTOA and CTOD values for DP600 base metal

Test number (coupon name)	True plastic strain at crack blunting	CTOA[a] (degrees)	CTOD[a] (mm)
BM1 (plate_base1_2)	28.66%	9.71	0.51
BM2 (plate_base2_1)	37.14%	9.27	0.46
BM3 (plate_base1_3)	32.95%	9.63	0.48
BM4 (plate_base2_2)	30.15%	9.67	0.49

[a] CTOA and CTOD threshold values are constant values extracted from the CTOD/CTOA vs. crack length curves such as those shown in Figs. 9(a), (b).

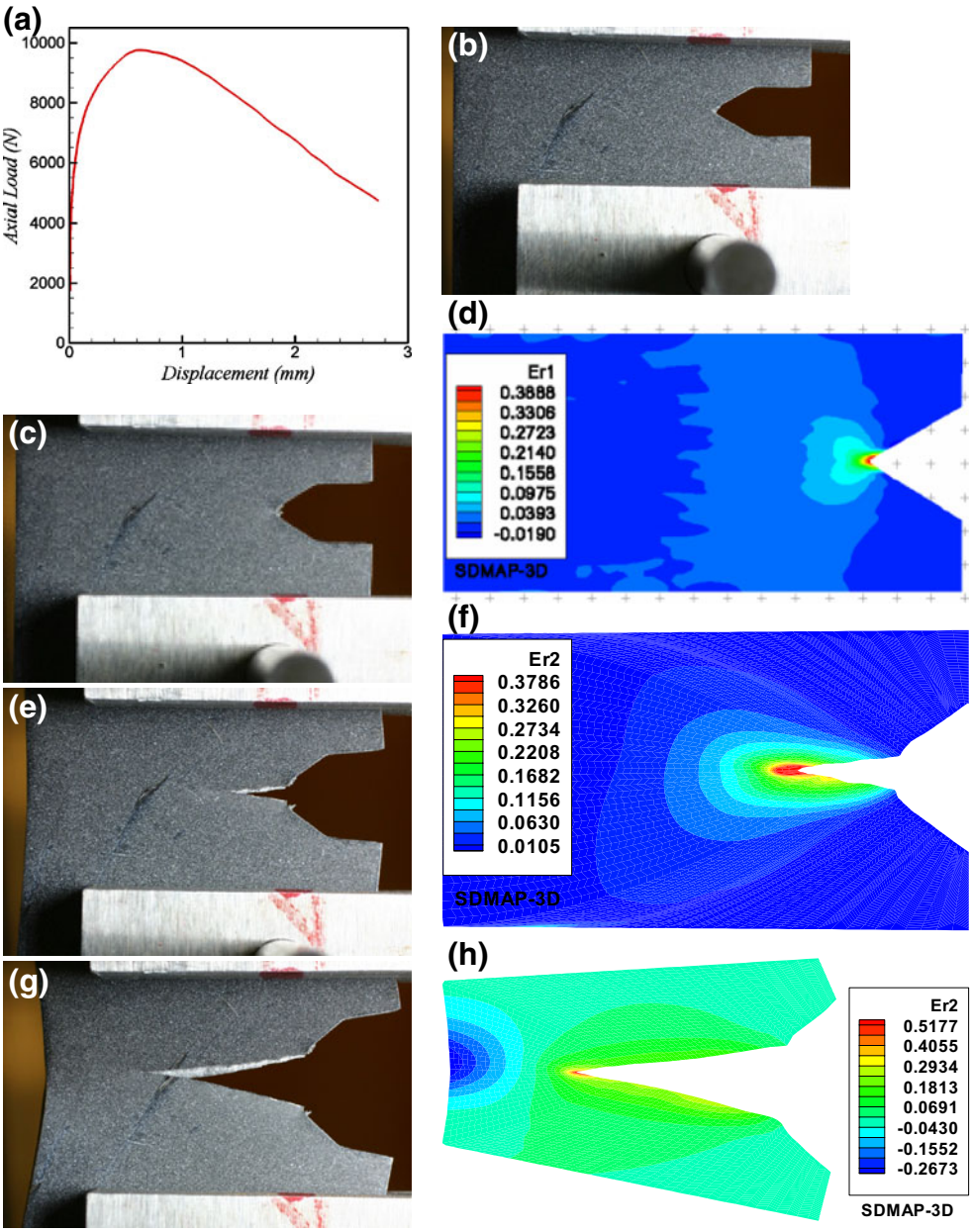

Fig. 7 Selected results of fracture test BM2 (base metal specimen No.2-1): (**a**) load-displacement curve; (**b**) undeformed image (#1655); (**c**) crack blunting (image #1690); (**d**) cumulative notch-tip strain field Er1 from the image pair of #1655 and #1690 (**e**) crack propagation (image #1720); (**f**) cumulative crack-tip strain field Er2 from the image pair of #1704 and #1720; (**g**) crack propagation (image #1760); (**h**) cumulative crack-tip strain field Er2 from the image pair #1704 and #1760. Er1 is the normal true strain in the horizontal X1-direction, and Er2 is the normal true strain in the loading direction or vertical X2-direction. Note that the strain contours in (d), (f) and (h) were computed with reverse DIC

To compute the CTOD/CTOA, the crack growth path was identified from deformed image #1728 (with a crack length of ~9.2 mm) and the undeformed image #1655 [Fig. 6(b)]. Image #1728, which is not shown in Fig. 7, was chosen as a suitable intermediate to images #1705 and #1760. After performing separate forward DIC analyses on the two regions in Fig. 6, the computed field data, which contains displacements, relative rotations, true axial strains (in the loading and transverse directions), and in-plane shear strains, were obtained. The DIC results are shown in Fig. 8. The processing region is shown in Fig. 8(a). Figure 8(b) shows the deformed boundary lines from DIC at the end of the test. Figures 8(c)–(f) show the computed cumulative displacement and strain fields in the deformed state. Note that U2 and U1 are displacements in pixel units along the loading direction and transverse to the loading direction, respectively, with 21.5 μm/pixel spatial resolution. The peak strain levels along the crack path in Fig. 8(e) are smaller than those for the crack tip [Figs. 7(f), (h)]. As shown in Fig. 8(f), the transverse strain along the crack growth direction was first negative, meaning that the specimen was under compression at the early stages of loading. Then the strain became positive, and hence the region around the crack growth path in the specimen was then under tension as the crack started to grow.

The variations of the CTOD and CTOA with crack length are shown in Figs. 9(a), (b). The CTOD first increased without crack propagation and then approached

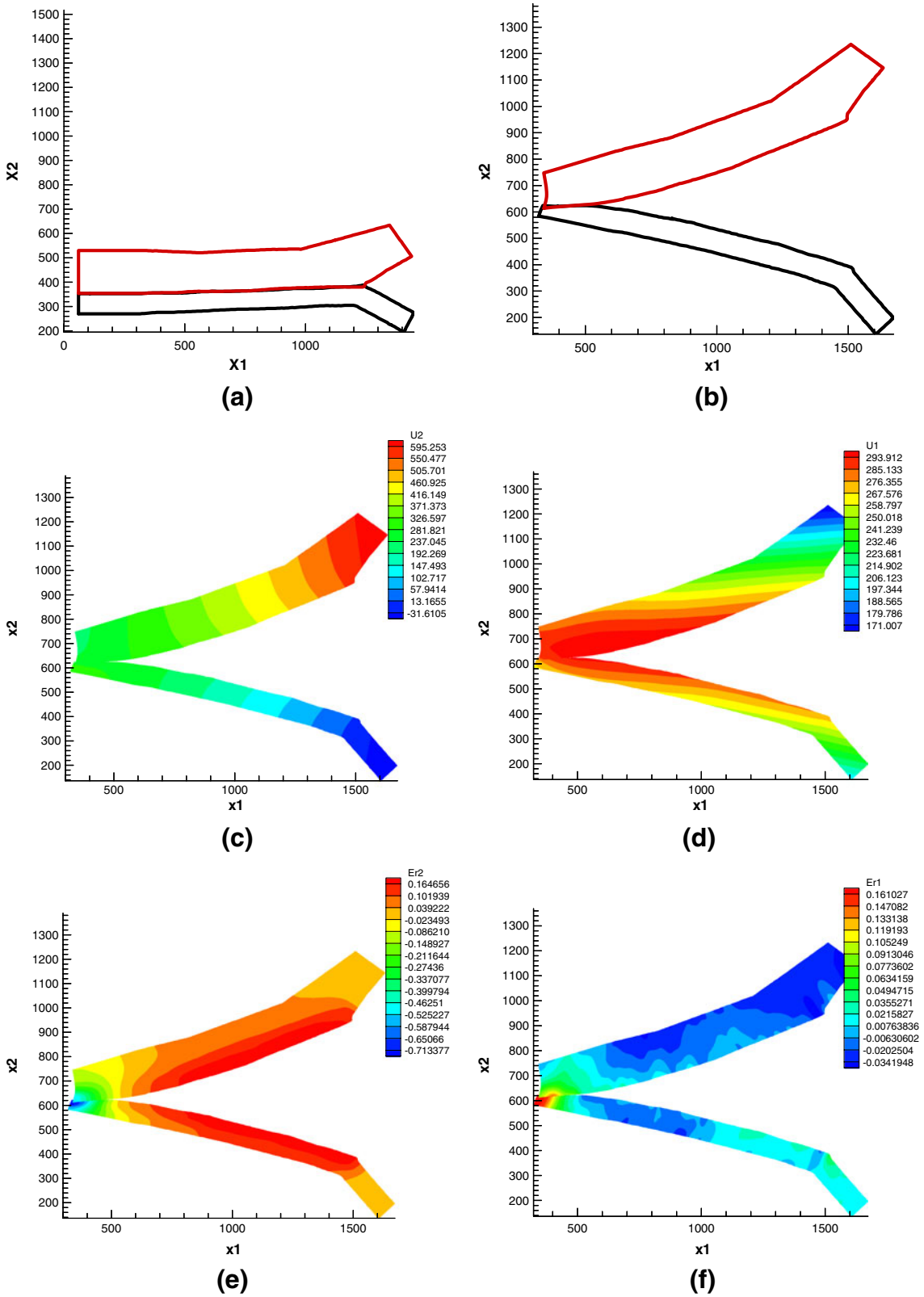

Fig. 8 Selected results of fracture test BM2 (base metal specimen No.2-1) for CTOD/CTOA measurement: (**a**) the two undeformed regions of interest as shown in Fig. 5(a) (image #1655); (**b**) the two deformed regions of interest (image #1805); (**c**) axial displacement U2 contour map in the loading direction; (**d**) transverse displacement U1 contour map; (**e**) true axial strain Er2 contour map (in the loading direction); (**f**) true transverse strain Er1 contour map

a steady state value of 0.46 mm with stable crack growth. The CTOA first increased to a value of ~16° and then tended to approach a steady state value of 9.27°. The NTOD and NTOA show a nearly linear variation with crack length in Figs. 9(c), (d), respectively. The NTOD does not achieve a constant value (as does the CTOD) since it is measured at the initial notch tip A/B in Fig. 5(a). However, the slope of the NTOD with crack tip length may in fact be nearly constant if the crack edges remain straight. The NTOA would also be constant if the crack edges remained straight. The fact it is not a constant indicates there is a bending effect that caused the crack edges to be slightly curved.

It is interesting to note that the value of the CTOA became (more or less) constant after a certain amount of crack propagation (~1.9 mm). The corresponding extent of crack propagation was of the order of the thickness (1.7 mm) of the V-notch tension specimen. This type of behavior may have resulted from the flat-to-slant transition. This is suggested in Fig. 7(g), where a white strip at the edge of the upper crack surface is visible. Here, the crack surfaces are not perpendicular to the loading axis. According to Anderson [58], when an edge crack in a plate grows by microvoid coalescence, the crack exhibits a tunneling effect where it grows faster in the center of the plate, rather than on the surfaces of the plate due to higher stress triaxiality [59–61]. There is thus a transition or change of fracture mode (from purely mode I to mixed mode I/III). Once crack propagation settled on a stable mixed mode fracture, then the CTOD became constant (more or less). In essence, crack tunneling is defined as the difference between the interior crack length and the surface crack length.

Welded Plates

Four welded V-notch tension samples were tested. Test results are summarized in Table 3. Each specimen is given a unique "SW" label (for "Spot Weld") in the first row of Table 3. The deformed test specimen SW3 is shown in Figs. 10(a), (b). Note that the spot weld is not evident due to the paint speckle coating necessary for DIC post processing of the strain fields. This specimen followed the geometry shown in Fig. 1(b) where the initial notch tip was positioned 1.5 mm above the fusion zone. When it was loaded (along the horizontal), the original notch tip first blunted, as shown in Fig. 10(a). Two stages of crack propagation then followed. In the first stage, which is shown in Fig. 10(b), the crack, which sits at the end of the white arrow in the figure, propagated straight down below the original notch tip. In the second stage, shown in Fig. 10(b), the direction of crack propagation changed to

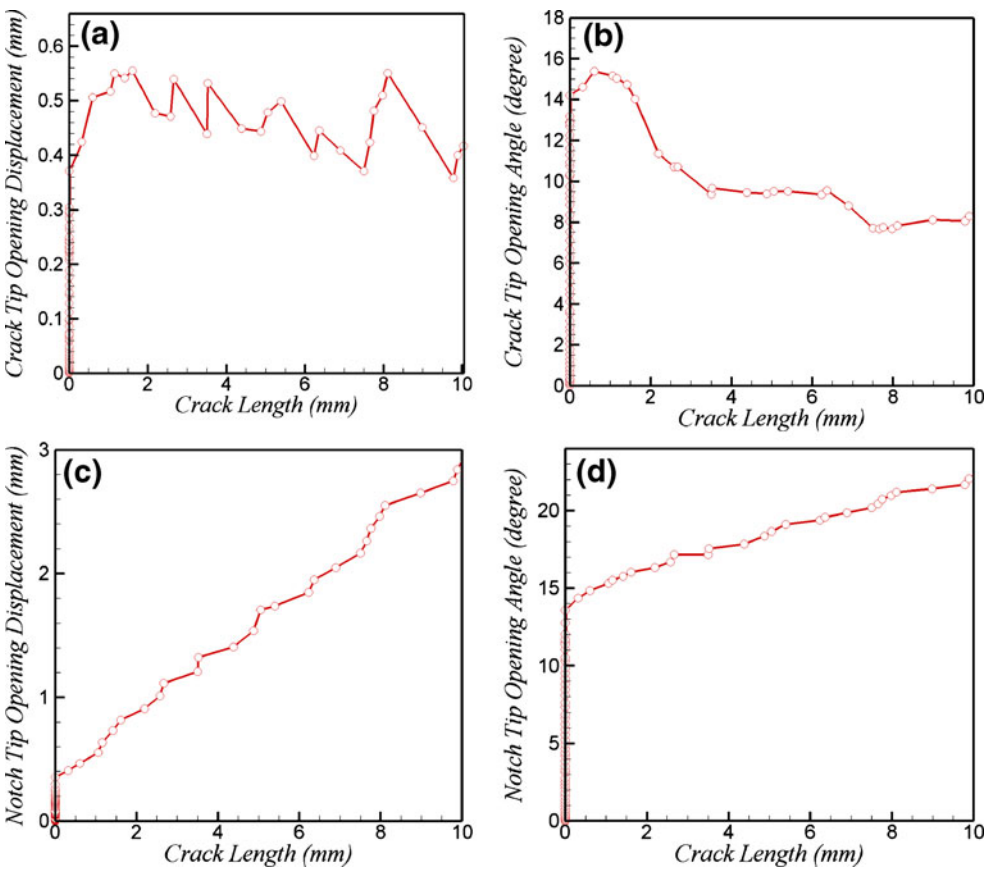

Fig. 9 Selected results of fracture test BM2 (base metal specimen No.2): (**a**) crack tip opening displacement (CTOD); (**b**) crack tip opening angle (CTOA); (**c**) notch-tip opening displacement (NTOD); (**d**) notch-tip opening angle (NTOA)

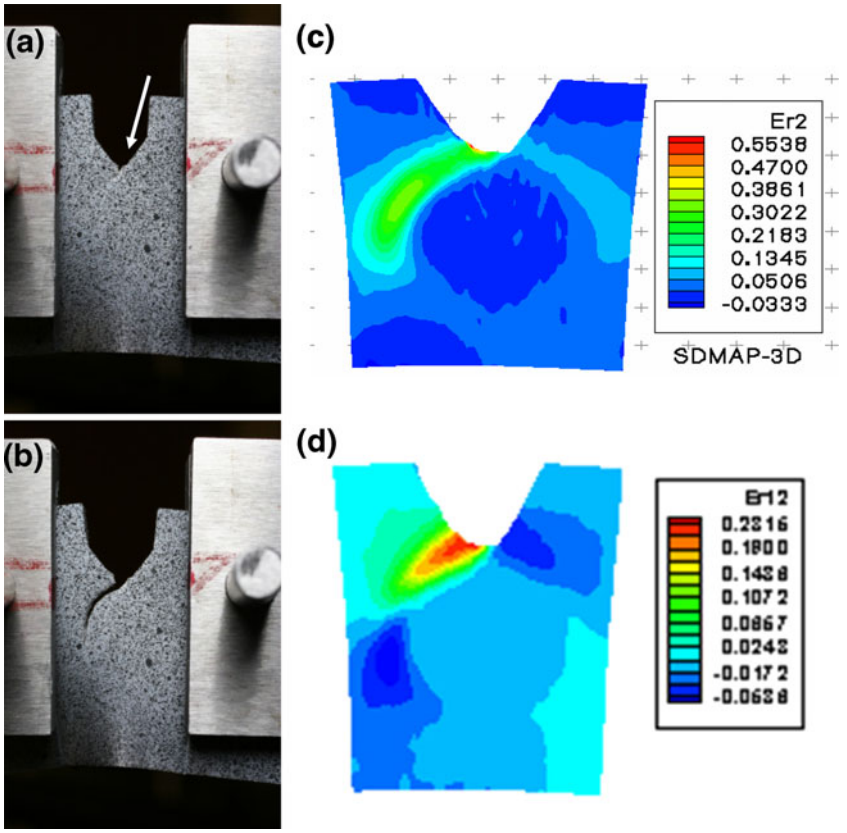

Fig. 10 Selected results of fracture test SW3 (spot-welded plate No.A3_1): (**a**) undeformed image (#646); (**b**) notch blunting (image #777); (a) white arrow points to the crack tip propagating towards the fusion zone (image #805); (b) curved crack propagation (image #825); (**c**) axial true strain Er2 contour map (images #646 vs. #777). (**d**) in-plane shear strain Er12 contour map (images #646 vs. #777). Note that the fusion zone is masked by the spray paint layer in (a)–(b)

follow a counterclockwise path around the circular fusion zone, bypassing it altogether. Additional study of the digital images of the crack process and associated SEM micrographs revealed that the crack grew into the base material and not into the HAZ. Even at the point of crack blunting, a plastic strain of ~32.5% had accumulated in the strains localized in the base material around the fusion zone region. This is shown as the light green contours with the contour lobe that runs counterclockwise in the axial strain map of Fig. 10(c). Shear strain contours are displayed in Fig. 10(d) and clearly show the direction of crack propagation. The highest shear strains along the crack path are ~22.2% and demonstrate that the DP600 spot weld fusion zone is resistant to mode I fracture altogether under the present testing conditions. This is not unexpected in light of the fact that the fusion zone consists primarily of martensite and there is no relative motion between the welded plates (as, for example, in tension-shear) in the mode I fracture test. The notch tip in fracture tests SW1 and SW2 followed the geometry in Fig. 1(c) and penetrated the fusion zone to a depth of 0.8~1 mm. When these specimens were loaded in the fracture tests, failure did not occur in the fusion zone either, even with the notch tip (with a certain stress concentration factor) penetrating it. Rather, the crack again followed a path around the fusion zone. No noticeable crack tip blunting was found inside the fusion zone in fracture tests SW1 and SW2. This suggests that a DP600 spot weld is resistant to mode I fracture loading irrespective of whether the notch tip is inside or outside of the fusion zone. The plastic strain around the region just outside of the fusion zone was consistently ~30% (as shown in Table 3) immediately prior to the failure occurring around it.

Summary Remarks

Strain fields in Mode I fracture studies of DP600 notch specimens consisting entirely of base material or containing a single spot weld were measured with the reverse DIC methodology. Since fracture involves the creation of new surfaces in the material, the usual forward DIC methodology, where one compares an image of the undeformed specimen with an image of the specimen in the deformed state, will not work. The reverse DIC methodology specifically addresses this issue by using the deformed state as the reference configuration to determine the location of the fracture surfaces

Table 3 Summary of fracture tests on dual-phase steel spot-welded plates

Test number (coupon name)	SW1 (A2_1)	SW2 (A2_2)	SW3 (A3_1)	SW4 (B2_2)
Plastic strain prior to failure around the weld	37.6%	33.2%	32.5%	28.3%

in the undeformed configuration. Subsequent cumulative correlation gives the crack tip deformation field due to the fracture process. Once the fracture surfaces are indentified, then forward DIC can be meaningfully applied to compute the deformation fields in the regions of solid material bounded by the crack surfaces and to measure the CTOD, CTOA, NTOA, and NTOD.

The measurement results detailed in this paper can be used to calibrate fracture models that account for material behaviors that are unique to DP600. This will be especially important for modeling purposes.

Of paramount importance is the measurement of crack tip deformation fields and the CTOD, CTOA, NTOA, and NTOD in the fusion zone of a DP600 spot weld. As long as the test configuration permits imaging of the propagating crack, either before and after the fracture process, or, preferably during fracture, then these measurements are entirely possible with reverse DIC. A technique that has yet to be explored to any significant detail and which could in fact provide digital images from which strain information could be extracted with reverse DIC is X-ray tomography.

Acknowledgments The authors are deeply grateful to B. Carlson for his critical review of an earlier version of the manuscript. The staff of the General Motors Test Hardware Engineering Group prepared designs of all test specimens used in this research. Warren Cavanaugh of the General Motors Pre-Production Operations cut all of the test specimens with wire electrical discharge machining.

References

1. Chen G, Chen XM, Shi MF, Kalpundi G, Wehner T, Yarlagadda R (2004) Material and processing modeling of dual phase steel front rails for crash, Proceedings of International Conference on Advanced High Strength Sheet Steels for Automotive Applications, June 2004, pp. 161–170
2. Chen XM, Shi MF, Chen G (2005) Crash performances of advanced high strength steels of DP780, TRIP780, and DP980, SAE technical paper # 2005-01-0354, SAE 2005 World Congress, April 2005, Detroit, MI
3. Horvath CD, Fekete JR (2004) Opportunities and challenges for increased usage of advanced high strength steels in automotive applications, Proceedings of International Conference on Advanced High Strength Sheet Steels for Automotive Applications, June 2004, pp. 3–10
4. Llewellyn DT, Hillis DJ (1996) Review: dual phase steel. Ironmak Steelmak 23(6):471
5. Rios PR, Guimaräes JRC, Chawla KK (1981) Modelling the stress-strain curves of dual phase steels. Scripta Mat 15(8):899–904
6. Gündüz S (2008) Static strain aging behaviour of dual phase steels. Mat Sci Eng A 486:63–71
7. Krauss G (1980) Principles of heat treatment of steel. American Soc. Metals (ASM), Metals Park, OH
8. Zhang S (2005) Simplified spot weld model for NVH simulations, SAE Paper #2005-01-0905
9. Marya M, Gayden XQ (2005) Development of requirements for resistance spot welding Dual-Phase (DP600) steels part 1 -The causes of interfacial fracture. Weld J 84(11):172-s–182-s
10. Tong W, Tao H, Jiang X, Zhang N, Marya M, Hector LG, Gayden XQ (2005) Deformation and fracture of miniature tensile bars with resistance spot-weld microstructures. Metall Mater Trans 36A:2651–2669
11. Tong W, Hector LG Jr, Tao H, Zavattieri PD (2008) Ductile fracture behavior of resistance spot-welded dual-phase steel. J Matls Eng Perf 17:517–534
12. Zhang J, Dong P (1998) Hybrid polygonal element method for fracture mechanics analysis of resistance spot welds containing porosity. Eng Fract Mech 59(6):815–825
13. Sun X, Stephens EV, Davies RW, Khaleel MA, Spinella DJ (2004) Effects of fusion zone size on failure modes and static strength of aluminum resistance spot welds. Weld J (Miami, Fla) 83(11):308-S–318-S
14. Zhang S (2001) Fracture mechanics solutions to spot welds. Int J Fracture 112:247–274
15. Zhang S (2001) Approximate stress formulas for a multiaxial spot weld specimen. Weld J (Miami) 80(8):201s–203s
16. Lin S-H, Pan J, Tyan T, Prasad P (2003) A general failure criterion for spot welds under combined loading conditions. Int J Solids Structures 40(21):5539–5564
17. Zuniga S, Sheppard SD (1997) Resistance spot weld failure loads and modes in overload conditions. ASTM Spec Tech Publ 1296:469–489
18. Radaj D (1989) Stress singularity, notch stress and structural stress at spot-welded joints. Eng Fracture Mech 34(2):495–506
19. Radaj D, Zhang S (1993) On the relations between notch stress and crack stress intensity in plane shear and mixed mode loading. Eng Fracture Mech 44(5):691–704
20. Zhang S (1997) Stress intensities at spot welds. Int J Fracture 88:167–185
21. Zhang S (1999) Stress intensities derived from stresses around a spot weld. Int J Fracture 99:239–257
22. Zhang S (1999) Approximate stress intensity factors and notch stresses for common spot-welded specimens. Weld J (Miami) 78 (5):1735–1795
23. Chao YJ (2003) Ultimate strength and failure mechanism of resistance spot weld subjected to tensile, shear, or combined tensile/shear loads. J Eng Matl Tech 125:125–132
24. Wung P (2001) A force-based failure criterion for spot weld design. Exp Mech 41(4):107–113
25. Wung P, Walsh T, Ourchane A, Stewart W, Jie M (2001) Failure of spot welds under in-plane static loading. Exp Mech 41(1):100–106
26. Lin S-H, Pan J, Wu S-R, Tyan T, Wung P (2002) Failure loads of spot welds under combined opening and shear static loading conditions. Int J Solids Structures 39(1):19–39
27. Lin S-H, Pan J, Wu S, Tyan T (2004) Failure loads of spot weld specimens under impact opening and sheer loading conditions. Exp Mech 44(2):147–157
28. Barkey ME, Kang H, Lee Y-L (2001) Failure modes of single resistance spot welded joints subjected to combined fatigue loading. Int J Mater Prod Technol 16(6–7):510–527
29. Lee H, Kim N, Lee TS (2005) Overload failure curve and fatigue behavior of spot-welded specimens. Eng Fracture Mech 72 (8):1203–1221
30. Marya M, Wang K, Hector LG Jr, Gayden XQ (2006) Tensile-shear forces and fracture modes in single and multiple weld specimens in dual-phase steels. ASME J Man Sci Eng 128:287–298
31. Liu S, Chao YJ, Zhu XK (2004) Tensile-shear transition in mixed mode I/III fracture. Int J Solids Structures 41(22–23):6147–6172
32. Smith BW, Li X, Tong W (1998) Error assessment for strain mapping by digital image correlation. Exp Tech 22(4):19–21
33. Tong W (1998) Strain characterization of propagative deformation bands. J Mech Phys Solids 46(10):2087–2102

34. Tong W (2004) Plastic strain mapping of bent sheets by image correlation. Exp Mech 44(5):502–511
35. Tong W (2004) An adaptive backward image correlation technique for deformation mapping of a growing crack in thin sheets. Exp Tech 28(3):63–67
36. Tong W (2005) An evaluation of digital image correlation criteria for strain mapping applications. Strain 41(4):167–175
37. Wells AA (1961) Unstable crack propagation in metals: cleavage and fast fracture. Proc. Crack Prop. Symp. Vol. 1, Paper 84, Cranfield, UK
38. Anderson H (1973) Finite element representation of stable crack growth. J Mech Phys Solids 21:337–356
39. De Koning AU (1977) A contribution to the analysis of quasi static crack growth in steel materials, in Proceedings, 4th nternational Conference on Fracture, University of Waterloo Press, 3, 25–31
40. Heerens J, Schroedel M (2003) On the determination of crack tip opening angle, CTOA, using light microscopy and δ_5 measurement technique. Eng Fracture Mech 70:417–426
41. Dawicke DS, Sutton MA (1994) CTOA and crack-tunneling measurements in thin sheet 2024-T3 aluminum alloy. Exp Mech 34(4):357–368
42. Mahmoud S, Lease K (2003) The effect of specimen thickness on the experimental characterization of critical crack-tip-opening angle 2024-T351 aluminum alloy. Eng Fracture Mech 70:443–456
43. Burton W, Mahmoud S, Lease K (2004) Effects of measurement techniques on the experimental characterization of crack tip opening angle- Δa resistance curves. Exp Mech 44(4):425–432
44. Tong W, Tao H (2004) Crack tip fields and fracture behavior in a NiTi shape memory alloy thin sheet. Mater Res Soc Symp Proc 785:D7.7.1–D7.7.6
45. Yan J-H, Sutton MA, Deng X, Cheng CC-S (2007) Mixed-mode fracture of ductile thin-sheet materials under combined in-plane and out-of-plane loading. Int J Fracture 144(4):297–321
46. Sutton MA, Yan J, Deng X, Cheng C-S, Zavattieri PD (2007) Three-dimensional digital image correlation to quantify deformation and crack-opening displacement in ductile aluminum under mixed-mode I/III loading. Opt Eng 46(5):051003
47. Wei Z, Deng X, Sutton M, Cheng C-S. A sub-region modeling approach for simulating mixed-mode fracture of ductile thin sheet under combined in-plane and out-of-plane loading, submitted
48. Poissant J, Barthelat F. A novel "subset splitting" procedure for digital image correlation on discontinuous displacement fields. Experimental Mechanics, doi:10.1007/s11340-009-9220-2
49. Gullerud AS, Dodds RH Jr, Hampton RW, Dawicke DS (1999) Three-dimensional modeling of ductile crack growth in thin sheet metals: computational aspects and validation. Eng Fracture Mech 63(4):347–374
50. Zuo J, Deng X, Sutton MA, Cheng C-S (2008) Three-dimensional crack growth in ductile materials; Effect of stress constraint on crack tunneling. J Press Vessel Tech Trans 130(3):0314011–0314018
51. Pratap CR, Pandey RK (1988) Evaluation of notch tip opening displacement using a composite crack profile approach. J Testing and Eval 16(1):17–21
52. Tong W, Zhang N (2004) On the crack initiation and growth in a strongly dynamic strain aging aluminum alloy sheet. J Mater Sci Technol 20(suppl 1):1–4
53. Minodai K, Kohnoi T, Shoichiro K, Waki Y (1982) Crack opening displacement characteristics of welded joint on low temperature service steel for LPG storage tanks. Trans ISIJ 22:942–951
54. Shi YW, Han ZX (1993) The effects of crack depth on the J-integral and CTOD fracture toughness for welded bend specimens. Fatigue Fract Eng Mater Struct 16:281–287
55. Datta R, Mukerjee D, Mishra S (1998) Weldability and toughness evaluation of pressure vessel quality steel using the Shielded Metal Arc Welding (SMAW) process. J Maters Eng Perf 7:817823
56. Meric C, Tokdemir M (1999) An investigation of the weld region of the SAE 1020 joined with metal active gas and determination of the mismatch factor. J Maters Eng Perf 8:601–605
57. Dawicke DS, Newman JC Jr., Bigelow CA (1995) Three-dimensional CTOA and constraint effects during stable tearing in a thin-sheet material. ASTM Special Technical Publication 223-242
58. Anderson TL (1995) Fracture mechanics fundamentals and applications, 2nd edn. CRC, Boca Raton
59. James MA, Newman JC (2003) The effect of crack tunneling on crack growth: experiments and CTOA analysis. Eng Fracture Analysis 70:457–468
60. Newman JC Jr, James MA, Zerbst U (2003) A review of the CTOA/CTOD fracture criterion. Eng Fracture Mech 70(3-4):371–385
61. Lan W, Deng X, Sutton MA, Cheng C-S (2006) Study of slant fracture in ductile materials. Int J Fracture 141(3–4):469–496
62. Helm J (2008) Digital image correlation for specimens with multiple growing cracks. Exp Mech 48:753–762
63. Oliver WC, Pharr GM (1992) An improved technique for determining hardness and elastic modulus using load and displacement sensing indentation experiments. J Mater Res 7 (6):1564–1583
64. Tao H (2006) Plastic deformation and fracture behaviors of resistance spot-welded Dual-Phase steel and Laser-Welded Aluminum sheet metals, Ph.D. Thesis, Department of Mechanical Engineering, Yale University, New Haven, CT